Microstructure and phase composition characterization in a $Co_{38}Ni_{33}Al_{29}$ ferromagnetic shape memory alloy

Reference:

Lu J.B., Schryvers Dominique.- Microstructure and phase composition characterization in a $Co_{38}Ni_{33}Al_{29}$ ferromagnetic shape memory alloy

Materials characterization - ISSN 1044-5803 - (2016), p. 1-18

Full text (Publishers DOI): http://dx.doi.org/doi:10.1016/j.matchar.2016.04.028

*Title Page

Microstructure and phase composition characterization in a $Co_{38}Ni_{33}Al_{29}$ ferromagnetic shape memory alloy

J.B. Lu[a,b], D. Schryvers[b*]

[a,b] School of Electronic and Information Engineering, Xi'an Jiaotong University, Xi'an 710049, People's Republic of China

[b] EMAT, University of Antwerp, Groenenborgerlaan 171, B-2020 Antwerp, Belgium

Corresponding author: Dominique (Nick) Schryvers
Email: nick.schryvers@uantwerpen.be
Tel: +3232653247
Fax: +32 32653318

Abstract

Transmission electron microscopy was performed to investigate the microstructures of a secondary phase and its surrounding matrix in a $Co_{38}Ni_{33}Al_{29}$ ferromagnetic shape memory alloy. The secondary phase shows a γ' $L1_2$ structure exhibiting a dendritic morphology with enclosed B2 austenite regions while the matrix shows the $L1_0$ martensitic structure. A secondary phase-austenite-martensite sandwich structure with residual austenite ranging from several hundred nanometers to several micrometers wide is observed at the secondary phase-martensite interface due to the depletion of Co and enrichment of Al in the chemical gradient zone and the effect of the strong martensitic start temperature dependency of the element concentrations. The crystallographic orientation relationship of the secondary phase and the B2 austenite fits the Kurdjumov-Sachs relationship.

Highlights:

- The secondary phase has a γ' $L1_2$ structure exhibiting a dendritic morphology.
- A secondary phase-austenite-martensite sandwich structure is observed.
- The structural sandwich structure is due to elemental composition variation.
- The secondary phase and the B2 austenite fit the Kurdjumov-Sachs relationship.

Microstructure and phase composition characterization in a $Co_{38}Ni_{33}Al_{29}$ ferromagnetic shape memory alloy

J.B. Lu[a,b], D. Schryvers[b*]

[a,b] School of Electronic and Information Engineering, Xi'an Jiaotong University, Xi'an 710049, People's Republic of China

[b] EMAT, University of Antwerp, Groenenborgerlaan 171, B-2020 Antwerp, Belgium

Corresponding author: Dominique (Nick) Schryvers

Email: nick.schryvers@uantwerpen.be

Tel: +3232653247

Fax: +32 32653318

Abstract

Transmission electron microscopy was performed to investigate the microstructures of a secondary phase and its surrounding matrix in a $Co_{38}Ni_{33}Al_{29}$ ferromagnetic shape memory alloy. The secondary phase shows a γ' $L1_2$ structure exhibiting a dendritic morphology with enclosed B2 austenite regions while the matrix shows the $L1_0$ martensitic structure. A secondary phase-austenite-martensite sandwich structure with residual austenite ranging from several hundred nanometers to several micrometers wide is observed at the secondary phase-martensite interface due to the depletion of Co and enrichment of Al in the chemical gradient zone and the effect of the strong martensitic start temperature dependency of the element concentrations. The crystallographic orientation relationship of the secondary phase and the B2 austenite fits the Kurdjumov-Sachs relationship.

Keywords

Microstructure; Transmission electron microscopy; Phase composition characterization; Ferromagnetic shape memory alloy

1. Introduction

Ferromagnetic shape memory alloys are drawing considerable interest owing to their potential applications as fast-responsive sensors and compact actuators [1-4]. In the past decades, the Co-Ni-Al system, characterized by its good ductility, high magnetocrystalline anisotropy energy as well as two ways shape memory effect, has been explored as a new member of ferromagnetic shape memory alloy (SMA) [5, 6]. It is well known that the B2 structure of paramagnetic Ni-Al alloys shows the shape memory effect [7]. With addition of Co this paramagnetic alloy changes into a ferromagnetic Co-Ni-Al SMA [8, 9], which is also viewed as a high temperature SMA as a result of its increased transformation temperatures [10], an extra advantage over the conventional binary system. The B2 structure of the β-phase of the Co-Ni-Al austenite alloy undergoes a martensitic transformation into a tetragonal $L1_0$ martensitic phase [11]. The magnetic Curie temperature (T_c) and martensitic transformation temperatures (start M_s or other) can individually be controlled in a wide range of 120K-420K by changing the concentrations of Co and Al [8]. Unfortunately, it is reported that Co-Ni-Al material only consisting of the single β-phase exhibits very poor ductility [8]. However, the presence of a secondary phase improves the hot fabricability and the high temperature ductility [8] [12], which implies an important advantage for practical applications. This secondary phase is a Co-rich fcc disordered γ- or $L1_2$ ordered γ'-phase, which homogeneously spreads in the matrix [11]. The two-phase alloy has a wide range of phase transition temperatures [8], where T_c and M_s depend on the annealing history due to the variation of chemical composition of the β-phase equilibrated with the γ- or γ'-phases [13]. Furthermore, mechanical properties measured with tensile and

bending tests were also reported to improve with an increase in the volume fraction of the secondary phase [14], whereas superelastic (SE) properties [13] and the shape memory effect [14] in the two-phase alloys strongly depend on the volume fraction of the secondary precipitates. In the annealed $Co_{38}Ni_{33}Al_{29}$ ferromagnetic shape memory alloy with specific pulling rate, apart from the dendritic secondary phase, micron-sized (up to 100 μm) fcc-based precipitates with partial γ' $L1_2$ ordering, and containing none, one or three $\{111\}_p$ parallel twin planes were found in the austenite matrix [15].

In addition, chemical concentration gradients across the phase boundaries were found to strongly affect the mechanical properties of SMA such as in precipitation-hardened maraging TRIP steel [16] and Ni-Ti multi-layer films [17]. The composition changes at the martensite-austenite interface in TRIP steel lead to the formation and growth of a new austenite layer on the existing retained austenite with drastically changed composition, which is expected to be responsible for the unexpected increase in ductility after the annealing treatment. In Ni-Ti multi-layer films, the films with chemical gradients have the added feature of an intrinsic two-way shape memory effect that greatly increases its potential functionality. Thus, the interphase microstructures of the $\beta+\gamma'$ two-phase Co-Ni-Al alloys are supposed to play an important role in the mechanical and physical properties of the system. In the current investigation, we will study the microstructure and chemical concentration across the interfaces by means of conventional, high-resolution and analytical TEM in a Co-Ni-Al ferromagnetic shape memory alloy.

2. Material and Methods

A $Co_{38}Ni_{33}Al_{29}$ ingot was obtained from Special Metals Corporation (New Hartford, NY). The ingot was melted and single crystals were grown by the directional Bridgman technique with a pulling rate of 28.8 $\mu m.s^{-1}$ in an Ar atmosphere, annealed at 1623K for 1h followed by water quenching.

Conventional TEM samples were prepared by twin-jet electropolishing in a 20% sulfuric acid and 80% methanol electrolyte at 258K [18]. In order to enable an adequate study of the matrix-secondary phase interfaces, an FEI Nova 200 Nanolab Dual Beam SEM/FIB system was applied to get cross-sections from the places of interest. A standard ion column is installed which allows Ga^+ milling at 5-30KV. Conventional TEM, high-resolution TEM and analytical STEM-EDX elemental line scan analyses were performed on a FEG FEI Tecnai G2 operated at 200KV. For the STEM-EDX analyses, spot size 6 was used yielding a 2-3 nm diameter beam spot. The α tilt of the sample was set to +15 degree to allow for a maximum X-ray collection. The spectra were collected and processed with Tecnai Imaging and Analysis software including background subtraction, peak fitting and thickness correction.

3. Results and Discussion

Fig. 1(a) shows a SEM image of the bulk sample, which reveals some details of the morphology of the sample with a dendritic structure of a micron-sized phase embedded in a martensitic matrix at room temperature. In this sample the secondary phase or the martensite-secondary phase interfaces do not reveal any particular crystallographic shapes or orientations. In order to investigate the nature of the secondary phase and martensite-secondary phase interface, a FIB lamella was prepared from the position indicated by the black bar.

Fig. 1(b) shows a bright field (BF) image of the FIB lamella taken along the $[100]_a$ zone axis of the austenite (the subscript “a” and “m” further-on in the text denote austenitic and martensitic structure, resp.). The right upper part exhibits the typical twinning structure of the martensitic phase. The selected area electron diffraction (SAED) pattern of the twin structure along the $[110]_m$ zone axis is shown in the right lower corner which consists of two sets of overlapping diffraction patterns. Each set of the pattern can be indexed by the typical $L1_0$ tetragonal martensitic structure with a=b=0.385nm, c=0.314nm [11]. The two sets of patterns share the spots along the $\mathbf{g}_{[1\text{-}11]m}$ direction, i.e. the diffraction spots along the $\mathbf{g}_{[1\text{-}11]m}$ direction are unsplit,

which indicates the twin plane (martensite plate boundaries) are the $(1\text{-}11)_{L10}$ planes. The small diffraction spots around the main spots might originate from surface martensite due to Ga^+ ion irradiation during FIB sample preparation [19, 20]. The middle part of Fig. 1(b) reveals the morphology of the austenitic phase. The corresponding SAED pattern taken along the $[100]_a$ zone axis is shown in the upper right corner, and can be indexed by the B2 cubic structure with a=0.285nm. Comparing the diffraction patterns of the austenite and martensite in Fig. 1(b), the expected orientation relationship $[100]_a||[110]_m$, and $(01\text{-}1)_a||(1\text{-}11)_m$ accompanying the martensitic phase transition and arising from a simple tetragonal distortion of the cubic cell can be confirmed. The left lower part of Fig. 1(b) reveals the morphology of the secondary phase with a slightly bend interface with the sandwiched austenite region.

Fig. 1(c) shows a HAADF-STEM image across the region of the secondary phase-austenite-martensite sandwich structure. The black line shows the trace along which a STEM-EDX line scan analysis with 45 detection positions, i.e. appr. one measurement each 40 nm, was performed. The characters *a*, *b* and *c* indicate the interface of secondary phase and austenite, the boundary of the chemical gradient zone in the austenite (see below) and the interface of the austenite and martensite, resp. Fig. 1(d) shows the concentration profiles of three elements across the sandwich structure. From these profiles we can clearly observe the Co depletion and Al enrichment in the *a*-*b* gradient zone compared with the *b*-*c* zone. For the present region, the width of this chemical gradient zone is around 200 nm, while other gradient regions in the sample were found to be between tens of nanometers to a maximum of 250nm. It is also important to mention that the size of the austenite, which is in the range of tens of nm to several micrometers, depends on the size and morphology of the secondary phase. The quantified mean EDX values of the different regions across the secondary phase-austenite-martensite sandwich structure are shown in Table 1. The data quantitatively show the presence of the Co depletion and Al enrichment in the *a*-*b* chemical gradient region, as well as a small composition difference between the austenite *b*-*c* and martensite regions. In addition, the concentrations of

Ni in the austenite and martensite are almost the same, about 10 at.% higher than in the secondary phase.

In order to interpret the formation of the secondary phase-austenite-martensite sandwich structure, the positions representing the element concentrations of different regions shown in Table 1 have been added to the Co-Ni-Al ternary phase diagram in Fig. 2 including the composition dependency of M_s [8]. The dash lines show the iso-contour temperatures of M_s, which indicate that M_s decreases with an increase of both Co and Al contents. For the martensite matrix, the composition indicates an M_s slightly below room temperature, which might indicate a certain systematic shift of the present measurements or of the phase diagram, probably due to the well-known very high sensitivity of M_s to composition in SMA. From the relative measures, however, it is clear that M_s (region *a*-*b*) < M_s (region *b*-*c*) < M_s (region martensite) where especially the two extreme cases properly explain the formation of the secondary phase-austenite-martensite sandwich structure. This means that the presence of the Co depleted and Al enriched chemical gradient zone and the composition difference between austenite and martensite result in a structure separation due to the strong dependency of M_s on alloy composition. Moreover, due to the orientation of the M_s iso-contour lines the changes in Al content play the most important role in this particular alloy. A similar phenomenon was reported in Ni-Ti shape memory micro-wire where the concentration gradient of the alloying elements stemming from the oxidation of the surface results in the formation of a martensite-austenite core-shell structure for the entire micro-wire [21].

However, the small difference in composition between the martensite and region *b*-*c* of the austenite does not explain the particular shape of the austenite region in this area. On the other hand, from the relative lattice orientation between austenite and martensite observed in Fig. 1, it is clear that the expected crystallography of the cubic-to-tetragonal transformation has been retained and the system will have to compete between the volume energy of both phases, governed by the concentration, and the surface energy at the habit plane induced by the

transformation strain. This has probably resulted in the particular hat-shape of the austenite-martensite interface in Fig. 1(b), yielding an austenite region slightly extending into an area with a higher Co and lower Al content.

Fig. 3(a) shows a SEM image of another area of bulk material. Besides the martensite variants recognized in the matrix, we can clearly observe a complicated dendritic structure of the secondary phase with the inclusion of some round and rod-shaped areas. In order to investigate the crystal structure and chemical information of the internal areas, a FIB cross-section lamella from the position indicated by the white bar was prepared. Fig. 3(b) shows the BF image of this FIB lamella, revealing a knife-shaped zone with some internal microstructure surrounded by the secondary phase. The majority of the diffraction patterns from this knife-shaped zone, as well as those from other internal areas between these dendritic structures, can be indexed by the B2 cubic austenitic phase. The fine twinning contrast in the center of the present austenite region stems from a small martensitic layer which is seen in overlap with the austenite.

The selected area electron diffraction (SAED) pattern from the interface of the austenite and secondary phase indicated by the white circle is shown in Fig. 3(c) and consists of two sets of diffraction patterns. One of them can be indexed by the austenite crystal structure along the $[111]_a$ zone axis while the other one by the secondary phase $L1_2$ crystal structure with a = 0.351nm along the $[110]_s$ zone axis as indicated by white arrows (the subscript “s” denotes secondary phase structure). It is clear that the diffraction spots along the $\mathbf{g}_{[-110]a}$(or $\mathbf{g}_{[-111]s}$) direction occur without splitting. Thus, the following orientation relationship between the austenite and secondary phase was found: $[111]_a//[110]_s$, $(-110)_a//(-111)_s$, which belongs to the Kurdjumov-Sachs relationship [15, 22]. Fig. 3(d) shows the HRTEM image of the interface corresponding to Fig. 3(c). Insets show the FFT images of the corresponding regions.

In order to investigate the chemical information of the austenitic phase, again quantitative EDX analysis was performed. The average element concentrations are shown in the last line of Table 1. The position indicated by a triangle corresponding to the composition is shown in Fig. 2, from which it is clear that the M_s of this area is far below room temperature explaining the austenitic phase formation inside the secondary phase. The small martensite area in the center of the zone of Fig. 3(b) is again the result of the competition between the volume and surface energy terms. The black arrow in the lower right corner of Fig. 3(d) indicates the presence of a stacking fault in the secondary phase. The stacking faults can influence the mechanical properties of the secondary phase, and as such have an impact on the overall mechanical properties of the alloy.

In some other samples of this same series, treated in slightly different ways, the secondary phase was found to be completely embedded in austenite matrix. Again some Co depletion and Al enrichment was observed in the matrix near to the secondary phase, but since the matrix is already in the austenite phase, no structural effect was induced by this concentration gradient.

4. Conclusions

Transmission electron microscopy and analytical techniques were performed to investigate the microstructure and local chemical concentration of a $Co_{38}Ni_{33}Al_{29}$ ferromagnetic shape memory alloy, which was grown with a pulling rate of 28.8 $\mu m.s^{-1}$, annealed at 1623K for 1h and then quenched in water. It was found that a dendritic-shaped secondary phase was almost homogeneously dispersed in a martensite matrix, with a secondary phase-austenite-martensite sandwich structure at the secondary phase-matrix interface structure and ranging from tens of nanometers to several micrometers in width. The formation of the sandwich structure can be explained by the presence of a Co-depleted and Al-enriched chemical gradient zone and the strong martensitic start temperature dependency on elemental composition. The austenite $[100]_a$ direction is found to be parallel to the martensite $[110]_m$ direction in this case, confirming

the origin of the sandwiched area as retained austenite. For the round and rod-like austenitic phase inside a dendritic structure of the secondary phase, the secondary phase and austenite fit Kurdjumov-Sachs orientation relationship. Several stacking faults were also observed in the secondary phase.

Acknowledgements

J.B. Lu thanks the Belgian Science Ministry (Belspo) for support of his post-doctoral research stay at EMAT. We thank S. Sedlakova-Ignacova from the Institute of Physics in Prague, Czech Republic, for providing samples.

References

[1] S. Takaoka, H. Horikawa, J. Kobayashi, K. Shimizu, Applications and development of shape-memory and superelastic alloys in Japan, Mater. Sci. Forum, 394-3 (2001) 61-68.

[2] N.B. Morgan, Medical shape memory alloy applications—the market and its products, Mater. Sci. Eng. A, 378 (2004) 16-23.

[3] T. Duerig, A. Pelton, D. Stöckel, An overview of nitinol medical applications, Mater. Sci. Eng. A, 273–275 (1999) 149-160.

[4] A.D. Johnson, Overview of thin film shape memory alloy applications in: Y.Q.F. Shuichi Miyazaki, Wei Min Huang (Ed.) Thin film shape memory alloys fundamentals and device applications, Cambridge University Press, 2009, pp. 261-274.

[5] O. Heczko, N. Scheerbaum, O. Gutfleisch, Magnetic shape memory phenomena, in: J.P. Liu, E. Fullerton, O. Gutfleisch, D.J. Sellmyer (Eds.) Nanoscale magnetic materials and applications, Springer US, 2009, pp. 399-439.

[6] A. Sozinov, A.A. Likhachev, N. Lanska, K. Ullakko, Giant magnetic-field-induced strain in NiMnGa seven-layered martensitic phase, Appl. Phys. Lett., 80 (2002) 1746-1748.

[7] K. Enami, S. Nenno, Memory effect in Ni-36.8 At. Pct Al martensite, Metall. Mater. Trans. B, 2 (1971) 1487-1490.

[8] K. Oikawa, L. Wulff, T. Iijima, F. Gejima, T. Ohmori, A. Fujita, K. Fukamichi, R. Kainuma, K. Ishida, Promising ferromagnetic Ni–Co–Al shape memory alloy system, Appl. Phys. Lett., 79 (2001) 3290-3292.

[9] Y. Murakami, D. Shindo, K. Oikawa, R. Kainuma, K. Ishida, Magnetic domain structures in Co-Ni-Al shape memory alloys studied by lorentz microscopy and electron holography, Acta Mater., 50 (2002) 2173-2184.

[10] G.S. Firstov, J. Van Humbeeck, Y.N. Koval, High temperature shape memory alloys problems and prospects, J. Intell. Mater. Syst. Struct., 17 (2006) 1041-1047.

[11] R. Kainuma, M. Ise, C.C. Jia, H. Ohtani, K. Ishida, Phase equilibria and microstructural control in the Ni-Co-Al system, Intermetallics, 4, Supplement 1 (1996) S151-S158.

[12] K. Ishida, R. Kainuma, N. Ueno, T. Nishizawa, Ductility enhancement in NiAl (B2)-base alloys by microstructural control, Metall. Mater. Trans. A, 22 (1991) 441-446.

[13] Y. Tanaka, K. Oikawa, Y. Sutou, T. Omori, R. Kainuma, K. Ishida, Martensitic transition and superelasticity of Co–Ni–Al ferromagnetic shape memory alloys with β+γ two-phase structure, Mater. Sci. Eng. A, 438–440 (2006) 1054-1060.

[14] T.O. Yuuki Tanaka, Katsunari Oikawa, Ryosuke Kainuma, Kiyohito Ishida, Ferromagnetic Co-Ni-Al shape memory alloys with β+γ two-phase structure, Mater. Trans., 45 (2004) 427-430.

[15] J.B. Lu, H. Shi, S. Sedlakova-Ignacova, R. Espinoza, J. Kopeček, P. Sittner, B. Bártová, D. Schryvers, Microstructure and precipitates in annealed $Co_{38}Ni_{33}Al_{29}$ ferromagnetic shape memory alloy, J Alloy Compd, 572 (2013) 5-10.

[16] O. Dmitrieva, D. Ponge, G. Inden, J. Millán, P. Choi, J. Sietsma, D. Raabe, Chemical gradients across phase boundaries between martensite and austenite in steel studied by atom probe tomography and simulation, Acta Mater., 59 (2011) 364-374.

[17] D.P. Cole, H.A. Bruck, A.L. Roytburd, Nanoindentation studies of graded shape memory alloy thin films processed using diffusion modification, J. Appl. Phys., 103 (2008) 064315.

[18] B. Bartova, D. Schryvers, Z. Yang, S. Ignacova, P. Sittner, Microstructure and precipitates in as-cast $Co_{38}Ni_{33}Al_{29}$ shape memory alloy, Scripta Mater., 57 (2007) 37-40.

[19] E. Zelaya, D. Schryvers, FCC surface precipitation in Cu-Zn-Al after low angle Ga+ion irradiation, Mater. Trans., 51 (2010) 2177-2180.

[20] E. Zelaya, A. Tolley, A.M. Condó, P.F.P. Fichtner, Ion irradiation induced precipitation of γ phase in Cu–Zn–Al–Ni, Mater. Sci. Eng., A, 444 (2007) 178-183.

[21] H. Tian, D. Schryvers, S. Shabalovskaya, J. Van Humbeeck, Microstructure of surface and subsurface layers of a Ni-Ti shape memory microwire, Microsc. Microanal., 15 (2009) 62-70.

[22] H. Fong, Chance occurrence of orientation relationships between phases in solid transformations and distribution of grain misorientations in a polycrystalline single phase material, Metall. Mater. Trans. A, 12 (1981) 2057-2062.

Figure captions:

Figure. 1 (a) Typical SEM image of the microstructural feature of the bulk sample, (b) BF image of FIB lamella taken along $[100]_a$ zone axis of residual austenite phase, (c) STEM image of the FIB lamella, (d) Concentration profiles of alloy elements across the secondary phase-austenite-martensite region shown in (c) using a STEM-EDX line scan method (each point corresponds with one measurement (per element) along the scan line).

Figure. 2 Observed concentrations in the sandwich structure in view of composition dependency of the martensitic start transformation temperature M_s in the Co-Ni-Al ternary system (after [8]).

Figure. 3 (a) SEM image of the bulk material showing the dendritic morphology of a γ' - secondary phase (white bar indicates the position where the TEM lamella was prepared by FIB, (b) BF TEM image of the FIB lamella, (c) Electron diffraction pattern taken from the area indicated by the white circle in (b) ($[111]_a$ / $[110]_s$), (d) HRTEM image of the interface of the secondary phase and austenite corresponding to (c) including some FFT patterns.

Table 1

The average element concentrations of different regions in Fig. 1(c), including statistical standard error values and number of measures per area (nb).

Positions (nb)	Co [at. %]	Ni [at. %]	Al [at. %]
Secondary phase (6)	52.28 ± 0.32	29.98 ± 0.15	17.74 ± 0.18
Region *a*-*b* austenite (7)	35.96 ± 0.58	33.85 ± 0.23	30.18 ± 0.41
Region *b*-*c* austenite (12)	37.89 ± 0.14	33.10 ± 0.20	29.00 ± 0.23
Region martensite (20)	38.33 ± 0.19	33.21 ± 0.19	28.44 ± 0.19
Area inside the secondary phase (Fig. 3) (5)	36.61 ± 0.42	32.94 ± 0.35	30.43 ± 0.27

Figure 1

Click here to download high resolution image

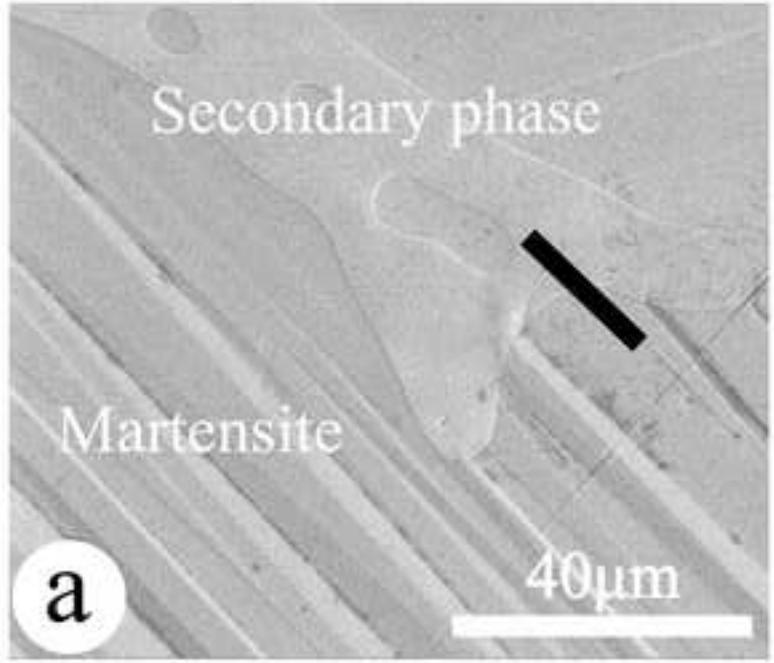

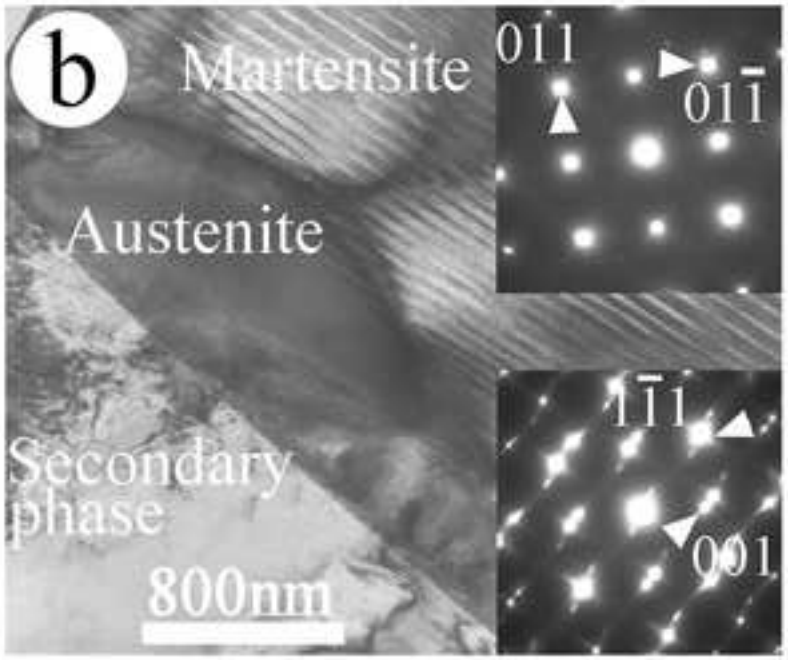

c

a : Interface of aus. and secondary phase
b : Chemical gradient boundary
c : Interface of aus. and mart.

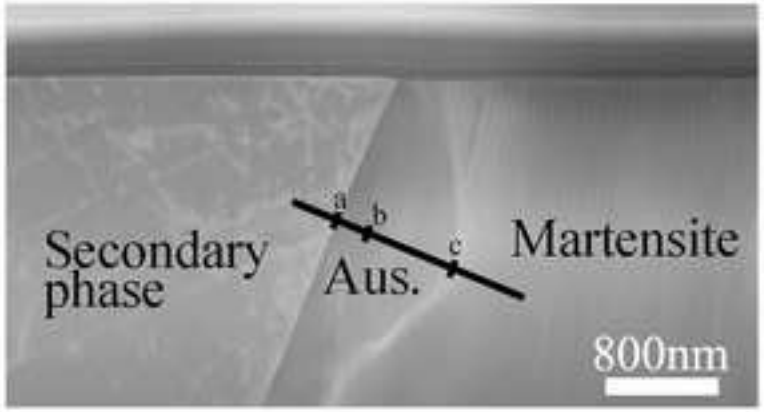

d

a : Interface of aus. and secondary phase
b : Chemical gradient boundary
c : Interface of aus. and mart.

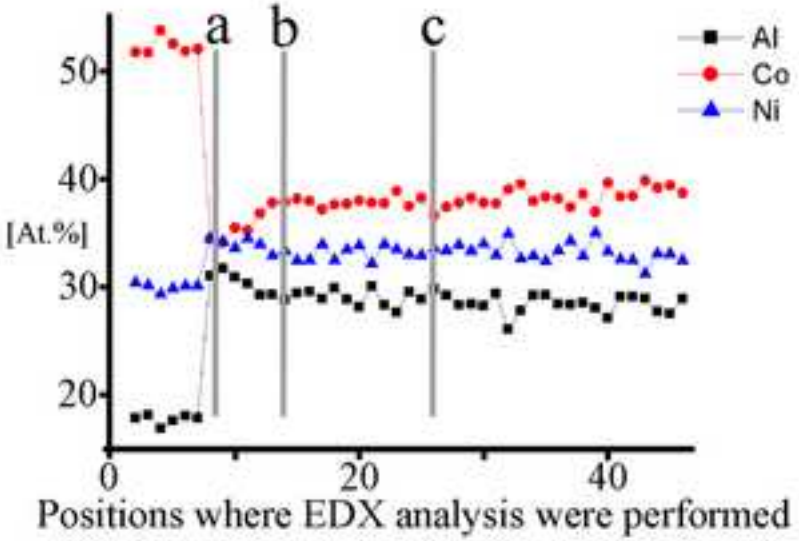

Figure 2
Click here to download high resolution image

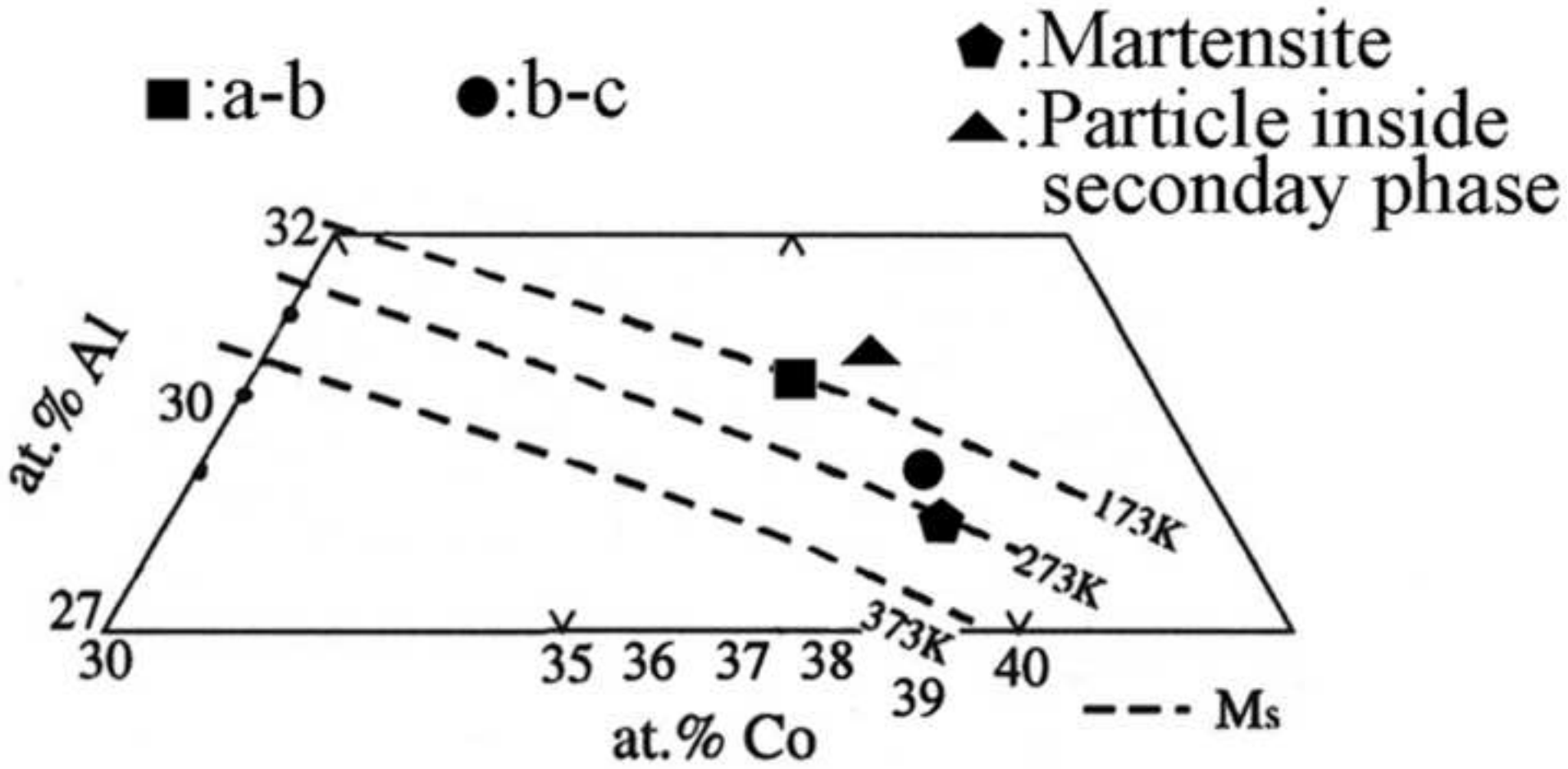

Figure 3

Click here to download high resolution image